# Relevance of Dzyaloshinskii–Moriya spectral broadenings in promoting spin decoherence: a comparative pulsed-EPR study of two structurally related iron( iii ) and chromium( iii ) spin-triangle molecular qubits

Jérôme Robert, Nathalie Parizel, Philippe Turek, Athanassios K Boudalis

ARTICLE

# Relevance of Dzyaloshinskii-Moriya spectral broadenings in promoting spin decoherence: a comparative pulsed-EPR study of two structurally related iron(III) and chromium(III) spin-triangle molecular qubits

Received 00th January 20xx,
Accepted 00th January 20xx

DOI: 10.1039/x0xx00000x

Jérôme Robert,[ab] Nathalie Parizel,[a] Philippe Turek,[a] Athanassios K. Boudalis*[a]

Spectral broadenings due to Dzyaloshinskii-Moriya interactions (DMI) were assessed with respect to the decoherence they induce through increased spin-spin interactions, as the role of DMI in developing magnetoelectric spin-chirality qubits is gaining recognition. The structurally related spin triangles $[Fe_3O(PhCOO)_6(py)_3]ClO_4{\cdot}py$ (**Fe$_3$**) and $[Cr_3O(PhCOO)_6(py)_3]ClO_4{\cdot}0.5py$ (**Cr$_3$**) were studied as frozen py-$d_5$ solutions with various pulsed Electron Paramagnetic Resonance (EPR) spectroscopy experiments, and under identical experimental conditions. Field-swept Hahn echo experiments revealed a match with continuous-wave (CW) spectra, while variable-temperature saturation/inversion recovery and Hahn echo decay experiments were used to extract the thermal evolutions of the spin-lattice relaxation and phase-memory times ($T_1$ and $T_m$, respectively). Nutation experiments revealed Rabi oscillations demonstrating that the spins of the complexes could be coherently manipulated. Careful comparisons of $T_M$ times confirmed hyperfine interactions with the magnetic nuclei of the metal ions as an intrinsic source of decoherence. Comparisons of Rabi damping times revealed that DMI-induced spectral broadenings play a discernible but moderate role as an extrinsic source of decoherence for the nutation experiments and that they are not particularly detrimental to spin manipulations.

## Introduction

Molecular Nanomagnets (MNMs) are potential candidates for spin qubits, with a major impetus being their attractiveness with respect to scalability and formation of nanoarrays through surface deposition. Indeed, several categories of MNMs have been considered as electron-spin qubits, such as Single-Molecule Magnets,[1,2] antiferromagnetic rings[3,4] or triangles[5–9] and mononuclear complexes.[10–15] A common problem of MNM-based electron-spin qubits is their rapid decoherence, mainly facilitated by magnetic noise due to hyperfine interactions with magnetic nuclei from ligands, counterions or solvents. Several strategies have been proposed to mitigate this problem.

A "brute-force" strategy consists in the creation of magnetically quiet environments through isotope engineering. The state of the art in this approach is the use of fragments from the "Avogadro crystal", a 5 kg isotopically ultrapure $^{28}Si$ single crystal, initially prepared for the redefinition of Avogadro's number;[16] $^{31}P$ donor atom implants in such a piece exhibited coherence times as long as 3 hours.[17] The molecular analogue of this strategy is the design of MNMs whose environments (ligands, solvents, counterions) either consist of elements which are naturally poor in magnetic isotopes (C, S), or are isotopically engineered to contain nuclei with small nuclear magnetic moments (e.g. $^2H$ instead of $^1H$). Using this approach, Freedman and coworkers reported a record coherence time of 675 μs for the mononuclear $(Ph_4P\text{-}d_{20})_2[V(C_8S_8)_3]$ (10 K in $CS_2$).[11] Though impressive, this result should be considered in conjunction with the fact that this approach severely restricts the synthetic flexibility that the use of MNMs promised to deliver in the first place. Moreover, reproducing the isotopic purity of the chemically simple "Avogadro crystal" in the chemically complex MNMs, could be prohibitively costly (encompassing the metal ions, ligands, counterions, and eventually solvents, of the entire synthetic process), as well as imperfect, as certain elements (e.g. hydrogen) do not have non-magnetic nuclei.

MNMs implementing nuclear-spin qubits have been projected to exhibit inherently slower decoherence due to their lower gyromagnetic ratios which protect them from magnetic noise due to weaker dipolar interactions. Since, however, this very feature would also hamper their efficient control, hybrid MNM qubits are considered, where a nuclear spin acts as the "client" qubit, carrying out information storage and processing, and a hyperfine-coupled electronic spin acts as the "bus" qubit assuring its external control and communication with other

[a] Institut de Chimie de Strasbourg (UMR 7177, CNRS-Unistra), Université de Strasbourg, 4 rue Blaise Pascal, CS 90032, F-67081 Strasbourg, France. E-mail: bountalis@unistra.fr.Address here.
[b] Sorbonne Université, CNRS, Laboratoire Jean Perrin, LJP, F-75005 Paris, France.
Electronic Supplementary Information (ESI) available: saturation & inversion recovery studies, determination of Debye temperature, Hahn echo decay and nutation studies. See DOI: 10.1039/x0xx00000x

qubits. This approach is best illustrated by the $[Tb(pc)_2]$ SMM, combining a $I$ = 3/2 nuclear spin and a $J$ = 6 ($S$ = 3, $L$ = 3) electronic spin of a $Tb^{III}$ ion, and which has been used as a qu*d*it[18] to implement Grover's algorithm on a single

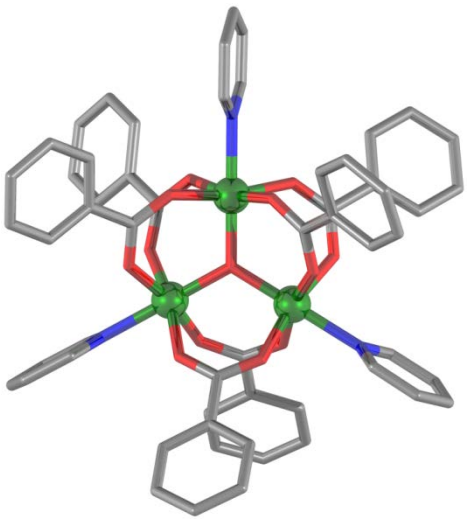

Figure 1. POV-Ray plot of the cation of complexes **$Fe_3$** and **$Cr_3$**.

molecule.[19] While such hybrid qubits have yielded phase memory times of a few tens of μs,[20–22] these remain quite below the record of $(Ph_4P\text{-}d_{20})_2[V(C_8S_8)_3]$, which might suggest that this strategy does not fully mitigate the effects of the nuclear spin bath.

A third approach, particularly adapted to MNMs with their large Hilbert spaces, is based on the prediction that working in carefully selected subspaces of the Hilbert space could insulate the spin qubits from magnetic noise and render them decoherence-free by design.[23] A proposed implementation of this strategy makes use of spin triangles characterized by a spin chiral texture, and consists in encoding the qubit states on the eigenvalues of their scalar spin chirality operator;[24,25] using the subspace spanning two spin levels with opposite scalar chiralities should shield them from magnetic noise when $\mathbf{B}_0||z$.[26] Moreover, due to their non-centrosymmetric structures, their spins were postulated to couple with external electric fields, thus allowing their direct electric manipulation, including their long-range coupling by microwave electric fields inside resonant cavities;[27] indeed this hypothesis has recently been confirmed for $[Fe_3O(PhCOO)_6(py)_3]ClO_4{\cdot}py$ (**$Fe_3$**) by us[28] and for a $Cu^{II}_3$ triangle by Liu et al.[29]

The lynchpin of this proposal is the existence of significant spin-orbit coupling, usually expressed as Dzyaloshinskii-Moriya interactions (DMI): not only are these interactions responsible for the development of spin chirality,[30,31] but are also expected to be relevant in mediating magnetoelectric coupling. However, DMI introduces important magnetic anisotropy in spin triangles, giving rise to extremely broad EPR spectra as we have reported in several cases.[32–35] Such spectral broadenings can introduce a significant source of decoherence through spin-spin interactions due to incomplete spectral excitations: given the small excitation window usually attainable by microwave pulses, excited triangles $M_3$* undergo dipole interactions with non-excited triangles $M_3$. The spin-lattice or spin-spin relaxations of $M_3$ can cause fluctuations in the local magnetic field of $M_3$* and accelerate their decoherence, over a process known as spectral diffusion.[36] Such an additional process can be an important driver of decoherence, even disregarding other mechanisms, such as hyperfine couplings, and irrespective of the considered information-storage scheme (e.g. spin chirality). It is therefore important to assess the relevance of DMI-induced spectral broadenings in promoting decoherence in spin triangles.

Despite the importance of spin triangles in the context of new spintronic materials, key parameters relating to their magnetic relaxation and spin decoherence properties remain ill-defined. Only a handful of such materials have been characterised through pulsed EPR techniques, with a single molecule studied in each case.[5–9] Spin nutations were described in only three studies,[5,6,9] while the effect of DMI in decoherence has not been considered despite its technological implications.

We have recently conducted detailed descriptions of the spin Hamiltonians of **$Fe_3$**[34] and its chromium(III) congener $[Cr_3O(PhCOO)_6(py)_3]ClO_4{\cdot}0.5py$ (**$Cr_3$**)[37] (Figure 1), which have revealed a ca. 40:1 respective ratio between the DMI strengths of the two (1.7 vs 0.041 $cm^{-1}$). These two complexes present, therefore, an ideal couple for conducting a strictly controlled comparative assessment of the effect of DMI-induced spectral broadenings in promoting decoherence in spin triangles. Herein, we present detailed pulsed EPR studies which elucidate the magnetic relaxation and decoherence properties of the two complexes and draw conclusions from their comparisons.

## Results

### Theoretical framework for the magnetic analysis of spin triangles

Spin triangles in general, and basic metal(III) carboxylates in particular, were the first MNMs for which the relevance of isotropic Heisenberg-Dirac-van Vleck (HDvV) exchange was understood and the spin Hamiltonian formalism applied.[38] To account for low-temperature magnetic susceptibility data, an equilateral-to-isosceles symmetry breaking was considered for the HDvV Hamiltonian,[39–41] better known as "magnetic Jahn-Teller effect",[42] which has also been considered in a dynamic context of atomic vibrations.[43,44] Low-temperature EPR data revealed the importance of DMI (antisymmetric exchange) in explaining their magnetic ($g$-tensor) anisotropy.[45–48] Numerous CW-EPR studies of transition-metal spin triangles have revealed a perpendicular $g$-tensor component ($g_\perp$) that gives rise to resonances at finite magnetic fields.[49,50] Its presence and position can be readily explained by assuming *both* an "isosceles" HDvV symmetry ($J_{12} = J_{13} = J$, $J_{23} = J' \neq J$) *and* a DMI-induced anisotropy. The relevant Hamiltonian is:

$$H = -2J(\hat{\mathbf{S}}_1\hat{\mathbf{S}}_2 + \hat{\mathbf{S}}_1\hat{\mathbf{S}}_3) - 2J'\hat{\mathbf{S}}_2\hat{\mathbf{S}}_3 - 2\mathbf{G}(\hat{\mathbf{S}}_1\times\hat{\mathbf{S}}_2 + \hat{\mathbf{S}}_2\times\hat{\mathbf{S}}_3 + \hat{\mathbf{S}}_3\times\hat{\mathbf{S}}_1) + \mu_B\mathbf{H}\Sigma\mathbf{g}_i\hat{\mathbf{S}}_i \quad (1)$$

in which the first two terms correspond to the isotropic HDvV exchange, the third term to DMI, and the last to Zeeman

interactions. To avoid overparametrization, a common DMI vector is considered for all spin pairs ($\mathbf{G}_{12} = \mathbf{G}_{23} = \mathbf{G}_{31} = \mathbf{G}$). Also, due to the symmetry of the molecules under study, the Moriya rules suggest that we may consider ($G_x$, $G_y$) ~ 0, i.e. $|\mathbf{G}| = G_z$. All these are illustrated in Scheme 1. This Hamiltonian can be also augmented with Hyperfine terms, depending on the metal ions and the experimental technique (e.g. EPR studies of $Cu_3^{II}$ triangles, or $^{57}$Fe Mössbauer studies of $Fe_3^{III}$ triangles); such terms were not considered in this study.

Other terms have also been tested, but their use has not met sufficient justification: single-ion zfs terms have been introduced, e.g. to explain the *g*-anisotropy of $[Fe_3S_4]^+$ centers in ferredoxins,[51,52] but they were subsequently shown to have a negligible effect in these centers[49] and in small molecules like **Fe$_3$**[34] and **Cr$_3$**;[37] higher-order biquadratic $(\hat{\mathbf{S}}_i\hat{\mathbf{S}}_j)^2$ and trilinear (three-body) $(\hat{\mathbf{S}}_i\hat{\mathbf{S}}_j)\cdot(\hat{\mathbf{S}}_j\hat{\mathbf{S}}_k)$ terms have also been considered[53] but disproved.[54]

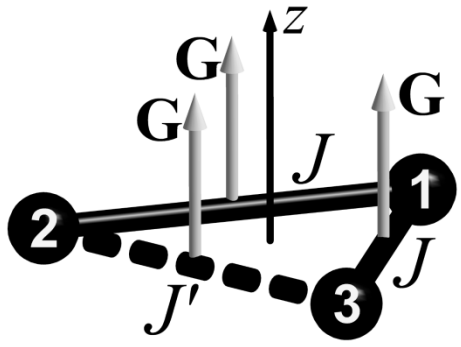


Scheme 1. Parameters of the "isosceles" spin Hamiltonian (1). Black spheres indicate metal ions. Black lines indicate HDvV coupling constants *J* (continuous lines) and *J'* (dashed line). Grey thick arrows indicate the DM vectors, assumed equal and parallel to the molecular *z*-axis (thin black arrow) which is normal to the triangle plane.

### Continuous-wave (CW) and field-sweep echo-detected (FSED) solution spectra

Powder/frozen solution CW-EPR spectra of spin triangles are typically axial, characterized by: (i) A low-field absorption-like feature which corresponds to the molecular orientation $z||\mathbf{B}_0$ ($g_{||}$), and whose value solely depends on the single-ion *g*-tensor elements. (ii) A higher-field derivative-like feature which corresponds to $z\perp\mathbf{B}_0$ ($g_\perp$) and whose value also depends on parameters $\Delta J = J - J'$ and $|\mathbf{G}|$.

The CW spectra of both complexes in frozen pyridine-$d_5$ solutions were qualitatively similar to the solid-state ones,[28,37] albeit presenting differences in the shape and width of their non-parallel part. The CW spectrum of **Fe$_3$** revealed resonances over a broad magnetic field range (3500-4500 G; *g* ~ 2.00-1.65), indicative of significant magnetic anisotropy, which is in line with the strong DMI ($G_z$ ~ 1.7-2.0 cm$^{-1}$) determined by solid-state studies. The spread of the signals is significantly reduced over that of the solid state[28] (where they reach up to 5500 G; *g* ~ 1.1), indicating the adoption of magnetic conformations in solution with significantly lower magnetic symmetries (larger $\Delta J$). The appearance of numerous resonances reveals magnetic conformations of different effective $g_\perp$ values. A similar, yet much more pronounced, narrowing is observed in the **Cr$_3$** complex which shows a spectral breadth of ~50 G (~3500-3550 G) greatly reduced with respect to the solid-state[37] (1.98-1.95 vs 1.98-1.5, respectively). This behavior is also in line with the characteristics of this complex previously published by us, indicating a much weaker DMI ($G_z$ = 0.041 cm$^{-1}$) inducing a much weaker magnetic anisotropy. Field-sweep echo-detected (FSED) pulse spectra are in excellent agreement with the CW ones, demonstrating that the echo observed is actually due to the sample.

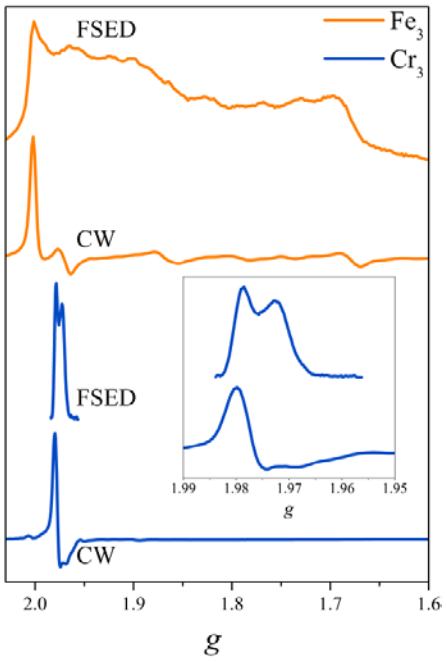


Figure 2. CW and FSED EPR spectra of **Fe$_3$** (orange) and **Cr$_3$** (blue) solutions in frozen pyridine-$d_5$ ($T$ = 4.40 K) plotted on a common *g* scale. The inset shows an expansion of the **Cr$_3$** spectra. CW and FSED spectra are plotted as first derivative and absorption spectra, respectively.

Before performing nutation experiments, we characterized the samples by measuring their intrinsic spin relaxation times, spin-lattice relaxation time $T_1$ and the phase memory time $T_M$: $T_1$ measures the lifetime of a classical bit, and $T_M$ measures the corresponding lifetime of a quantum bit, encoded in the phase of the quantum state.

### Spin-lattice relaxation

Initial attempts to measure the $T_1$ time of **Fe$_3$** with inversion-recovery experiments were inconclusive, as the relaxation profiles could not be satisfactorily fitted to simple exponential law $M(t) = M_0(1-2e^{-(t/T_1)})$, due to incomplete inversion of the magnetizations, reaching only -0.8$M_0$ for **Fe$_3$** (Figure S3) and -0.2$M_0$ for **Cr$_3$** (Figure S4) at the lowest temperatures. This was attributed to spectral diffusion due to the broad linewidths, and the inversion recovery traces of **Cr$_3$** could be well reproduced by a stretched exponential law, $M(t) = M_0(1-2e^{-(t/T_1)^\beta})$. However, this approach was still ineffective for **Fe$_3$**. To remedy this, and to assure the comparability of the results, saturation recovery measurements were carried out for both complexes (Figures S1 and S2), preceded by a picket-fence excitation. These

yielded decay profiles that could be better fitted to simple exponential decay laws, and are the ones discussed here.

A monoexponential fit according to $M(t) = M_0(1-e^{-(t/T_1)})$ (2) yielded satisfactory results, however it was found that these were improved by inclusion of a spectral diffusion component, or by consideration of a stretched exponential law. A stretched exponential law $M(t) = M_0(1-e^{-(t/T_1)^{\beta}})$ (3) yielded much better results than the inclusion of the spectral diffusion term, with $\beta$ ~ 0.6-0.7, indicating significant distributions of the relaxation times. Saturation recovery curves recorded at variable temperatures revealed that the relaxation was temperature-independent below 5.5 K for **Fe$_3$** and below 6 K for **Cr$_3$**, characteristic of a direct process,[55] possibly influenced by a phonon bottleneck. Above these temperatures, and up to the temperature where an echo was no longer observable (8 K for **Fe$_3$**; 7.5 K for **Cr$_3$**), the thermal evolution of $1/T_1$ was logarithmic with respect to $1/T$.

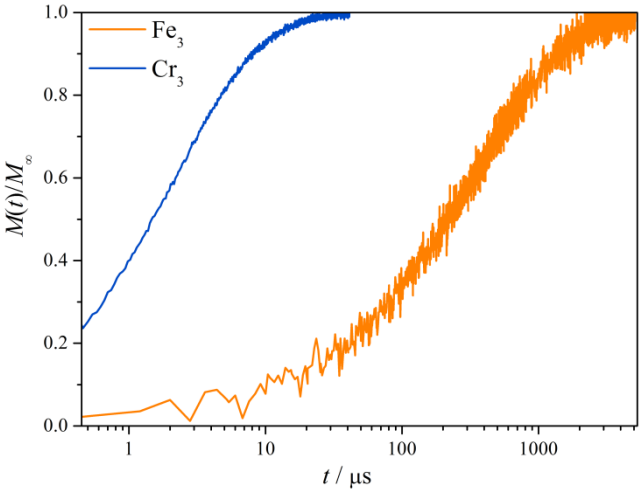


Figure 3. Indicative saturation recovery traces for **Fe$_3$** (4.13 K) and **Cr$_3$** (4.40) showing the differences in spin-lattice relaxation times which differ by more than three orders of magnitudes.

Spin-lattice relaxation at very low temperatures is usually dominated by the direct single-phonon process, whose temperature dependence is described by the relation $T_1^{-1} = C\coth(g\mu_B H/k_B T) \sim AT$ (4), while phonon bottlenecks may arise at these temperatures, when the phonons emitted by direct processes cannot be dissipated by the heat bath and are reabsorbed by the spins.[56] At intermediate temperatures, and if there are low-lying states, the phonon spectrum can activate the two-phonon Orbach process, which proceeds via the excited states accessible to the phonon energies at these temperatures and is described by $T_1^{-1} = b_O\Delta^3[1/(e^{\Delta/T} - 1)] \sim b_O\Delta^3 e^{-\Delta/T}$ (5). The Orbach process can also be fitted to the Arrhenius equation $T_1^{-1} = T_{1(0)}^{-1} e^{-\Delta/T}$ (6), which allows a useful comparison between the pre-exponential factors reported for various paramagnetic systems. A competing process at those temperatures is the second-order Raman process, whose temperature dependence can vary widely depending on the system, and which can be hard to distinguish from the Orbach process. For Kramers systems in crystals, the Raman process it is usually found to satisfy the thermal dependence $T_1^{-1} = b_R I_8 T^9$ (7), where

$$I_8\left(\frac{\theta_D}{T}\right) = \int_0^{\theta_D/T} x^8 \frac{e^x}{(e^x-1)^2}\,dx$$

which simplifies to $I_8 = 8!$ for $T << \vartheta_D$, leading to a thermal dependency to $T^9$.[57] However, Kramers systems in proteins were found to exhibit a decrease in the spectral dimension, leading to thermal variations of $T_1^{-1} = b_R' T^x$ (8), with $x < 9$.[58]

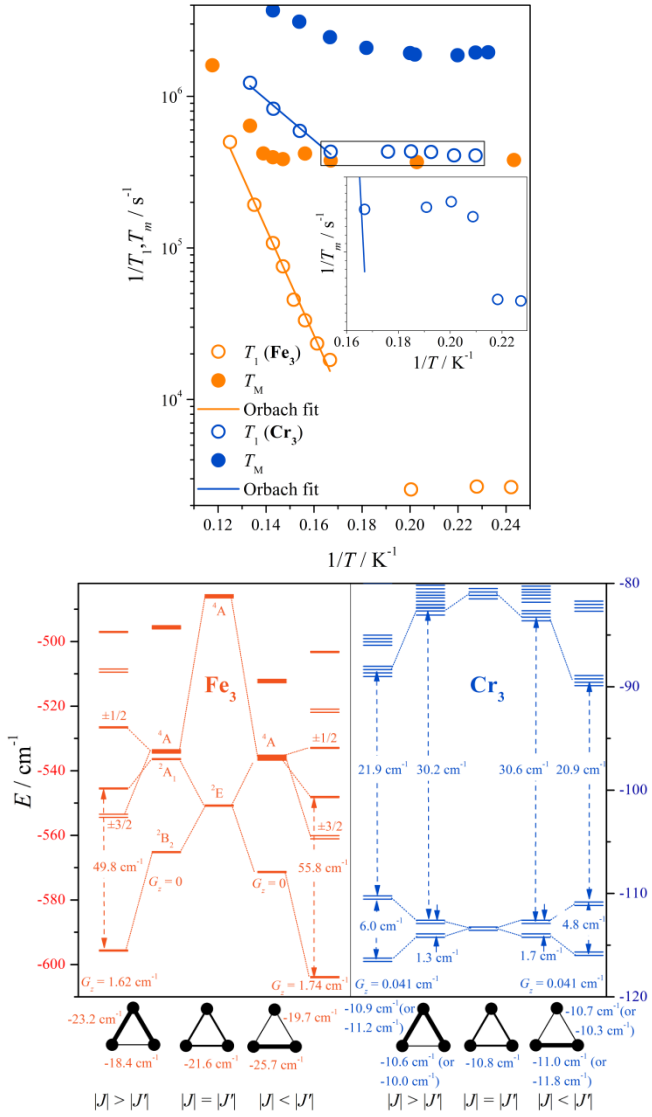


Figure 4. **Top:** $T_1$ (●) and $T_M$ (○) data derived from stretched exponential fits to the saturation recovery traces of **Fe$_3$** (orange) and **Cr$_3$** (blue), with fits to the low-$T$ $T_1$ data to Orbach processes. The inset shows an enlargement of the **Cr$_3$** low-$T$ data as outlined by the rectangle frame, which reveals a stepped feature in $T_1$ variation. **Bottom:** Low-lying energy levels calculated for **Fe$_3$** (orange) and **Cr$_3$** (blue) from the spin Hamiltonian parameters determined in references [34] and [37], including the Zeeman splitting at the magnetic field of the pEPR experiments (**Fe$_3$**: 3475 G, $g$ = 2.00; **Cr$_3$**: 3515 G, $g$ = 1.98). In the case of **Fe$_3$**, the diagram shows the energy shifts induced during the progression from the equilateral model ($|J| = |J'|$) to the two isosceles ones ($|J| > |J'|$, left; $|J| < |J'|$), right), in the fully isotropic ($G_z = 0$, inner plots) and anisotropic ($G_z \neq 0$, outer plots) cases. The plots reveal the zfs induced to the quartet states by DMI. In the case of **Cr$_3$**, where DMI is very weak, the plots show the progression from the equilateral (center plot), to weakly (inner plots) and strongly isosceles-distorted models (outer plots). The cartoons at the bottom illustrate the type of magnetic symmetry by associating the line thicknesses to the $J$ strengths. $J$ values are selected so that $J_{av} = (2J + J')/3$ is the same between equilateral and isosceles models.

While such subtle distinctions are generally difficult, especially for exchange-coupled systems with relaxation data spanning very narrow temperature ranges, comparative studies of the two complexes allow us to derive meaningful conclusions. Attempts to fit the high-*T* relaxation data to a Raman process described by (2) were unsuccessful, requiring unrealistically low Debye temperatures for either sample (~30-40 K), and failing to reproduce the slope of the high-*T* data for **Fe$_3$**. Relaxing the constraints of the spectral dimension, to account for the fact that the samples are not crystalline but frozen solutions, fits to (8) gave satisfactory fits (see parameters in Table 1), but with highly varying *x* values (~12 for **Fe$_3$** and ~4 for **Cr$_3$**).

Table 1. Fits of the high-*T* data to Orbach and Raman models

| | | Orbach | | | Raman | |
|---|---|---|---|---|---|---|
| | | $T_{1(0)}$ (s) | $b_O$ ($10^3$ $s^{-1}$ $K^{-3}$) | Δ ($cm^{-1}$) | $b_R'$ ($s^{-1}$ $K^{-x}$) | *x* |
| **Fe$_3$** | Monoexp. | $8.00\times10^{-11}$ | 23.2 | 56(2) | $1.08\times10^{-5}$ | 11.8(4) |
| | Stretched | $8.58\times10^{-11}$ | 21.8 | 56(2) | $1.07\times10^{-5}$ | 11.8(2) |
| **Cr$_3$** | Monoexp. | $1.64\times10^{-8}$ | 2.16 | 20(1) | 168 | 4.4(2) |
| | Stretched | $1.39\times10^{-8}$ | 2.44 | 22(1) | 105 | 4.6(2) |

Since the main driver of the Raman process is the system's Debye temperature, which is expected to be very similar for both samples, i.e. close to that of the host solvent (235 K for the I polymorph of frozen pyridine-$d_5$[59]), we expect that the striking differences in relaxation characteristics are due to other factors (the Debye temperature for the **Fe$_3$** complex in the solid state was determined from previously reported data as 199 K, i.e. close to that of the sample solvent; see SI for calculations). Moreover, considering the magnetic structures of the two complexes, we calculate that $k_B\Theta_D$ ~ 140-160 $cm^{-1}$ > $\Delta_{Fe3}$ (50-60 $cm^{-1}$) >> $\Delta_{Cr3}$ (2-3 $cm^{-1}$), which strongly favors the Orbach process at the considered temperature ranges.[57] Relations (5) and (6) are closely related and their use yielded identical activation energies for the Orbach process of either complex. The pre-exponential factors for **Fe$_3$** (~$8\times10^{-11}$ s) in the Arrhenius representation are remarkably similar to the values we derived for the same complex in the solid state using ac-susceptometry.[33] The values derived for $b_O$ in the Orbach representation are also in general agreement with those of $Fe_3$-salox[5], for which an Orbach process had also been observed; however these are significantly higher than those derived for the magnetically related $[Fe_3S_4]^+$ active sites of ferredoxins.[60] On the other hand, these are the first such values reported for a $Cr^{III}$ triangle.

Regarding the activation energies, these are in excellent agreement with the spin Hamiltonian parameters previously determined for **Fe$_3$**[34] and in good agreement with those determined for **Cr$_3$**[37] in the solid state (Figure 4).

As can be seen, the extracted activation energies for **Fe$_3$** agree very well with the energy of the first excited $M_S$ = ±1/2 Kramers doublet. In the case of solution (*J*, *J'*) = (-23.2 $cm^{-1}$, -18.4 $cm^{-1}$), this is the $|S_T = 1/2, M_s = \pm1/2\rangle$ state of the excited doublet, however, in the case of solution (-19,7 $cm^{-1}$, -25.7 $cm^{-1}$) this is the $|S_T = 3/2, M_s = \pm1/2\rangle$ stemming from the first quartet state, which also happens to be the first excited state for that magnetic symmetry. It should be noted that for the Dzyaloshinskii-Moriya parameters determined from those fits, the zero-field splittings imparted to the quartet state are so strong that the $M_S$ = ±3/2 Kramers doublet is always the first excited state. However, this doublet should not participate in the relaxation process since, apart from the phononic excitation, this would require an additional $\Delta M_S$ = +1 or -2 spin flip.

As far as the **Cr$_3$** complex is concerned, the previously reported solid-state best-fit parameters yield an energy gap about 50% larger than the extracted activation energies. As previously mentioned, the much narrower EPR spectra recorded in frozen solutions indicate a decrease of the magnetic symmetry with respect to the solid state (i.e. $|\Delta J|_{soln}$ > 0.3 $cm^{-1}$). Indeed, 0.3-0.8 $cm^{-1}$ variations of the $J_{ij}$ values (Δ*J* values of +1.5 or –1.2 $cm^{-1}$) induce energy separations of ~21 $cm^{-1}$ between the excited doublet and the first quartet state, in agreement with the relaxation activation energy. Such an energy spectrum could also involve an additional Orbach process of a 5-6 $cm^{-1}$ activation energy which would be accessible by lower-energy phonons and which should be operative at lower temperatures. This would be in line with the step-like feature of the low-*T* data.

The above considerations indicate that an Orbach mechanism is dominant in the spin-lattice relaxation above 6 K. However, the very different $T_1$ times at the low-*T* temperature-independent regime, where Orbach processes are still inactive, indicate that additional factors influence the relaxation dynamics and render the spin-lattice relaxation of **Cr$_3$** more efficient. An indication to that effect might also be the widely varying $b_O$ (or $T_{1(0)}$) values, although such a comparison is complicated by eventual correlations of the fitting parameters.

**Spin-spin relaxation**

The Hahn echo decay was monitored to determine the value of $T_M$. The strong oscillations in the echo decay signals of both complexes are electron spin-echo envelope modulation (ESEEM) caused by coupling to deuterium nuclear spins of the pyridine. The Fourier transform of the Hahn echo decay (Figure S6) well confirms the existence of these hyperfine interactions with the presence of the peaks at 2.2 MHz ($\nu_D$) and 4.4 MHz ($2\nu_D$). To determine $T_m$, an exponential fitting was carried out, including a ~2.2 MHz modulation term to account for the effects of hyperfine couplings, based on the equation:[61]

$$I(\tau) = I(0) + A_{2p}e^{-2\tau/T_M}\left[1 + ke^{-(2b\tau)^2}\cos(2\pi\nu\tau + \varphi)\right]$$

Fits are presented in Figure 5, and best-fit parameters are given in Table S2 and plotted in Figures 4, S6 and S7.

These results for **Fe$_3$** compare remarkably well with the $T_M$ times reported for a related $Fe_3$-salox complex.[5] No other studies on the decoherence properties of $Cr^{III}$ triangles have been carried out so far, although several exchange-coupled

$Cr_7M$ rings have been previously studied, exhibiting $T_M$ times at the same range, i.e. 0.86 µs for $M^{II}$ = $Zn^{II}$,[62] 0.34-3.8 µs for $M^{II}$ = $Ni^{II}$,[4,63–66] and 0.55 µs for $M^{II}$ = $Mn^{II}$.[63]

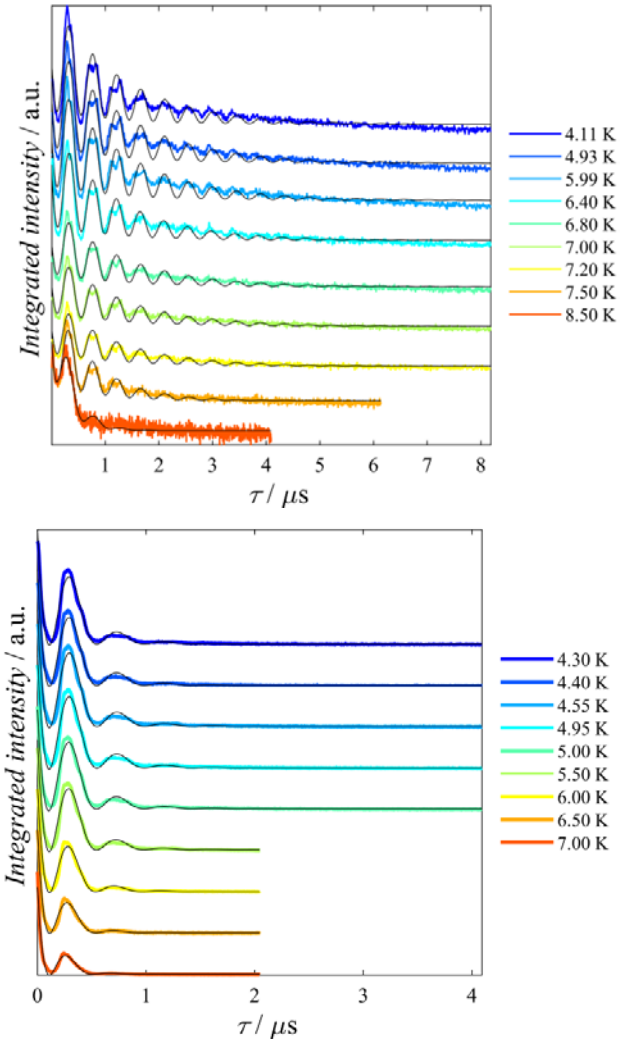


Figure 5. Hahn echo decay experiments for **$Fe_3$** (top panel) and **$Cr_3$** (bottom panel) at variable temperatures (coloured lines). The black lines correspond to fits according to the model described in the text.

### Nutation experiments

Despite the recent interest of spin triangles as molecular qubits, Rabi oscillations, i.e. the coherent driving of electrons between the two Zeeman-split energy levels, have only been demonstrated in three cases.[5,6,9] Rabi oscillations exemplify the ability to manipulate spins both for spintronics and quantum information processing. The capacity to rotate the qubits arbitrarily to any point on the Bloch sphere is one of the two main requirements for creating universal quantum gates, the other being the ability to entangle qubits.

To assess the possibility to coherently drive the spins of spin triangles, nutation experiments were carried out. The delays and pulse durations of the nutation Rabi sequence (Figure 6) were chosen in function of the values of the previously measured times $T_M$ and $T_1$ (see Experimental). The frequency of the oscillations of the signal depends on the magnitude of the magnetic field $\mathbf{B}_1$ and on the total spin of the sample's ground state, according to the relation:

$$\nu_{nut} = \frac{\mu_B g B_1}{\hbar}\sqrt{S(S+1) - M_s(M_s+1)}$$

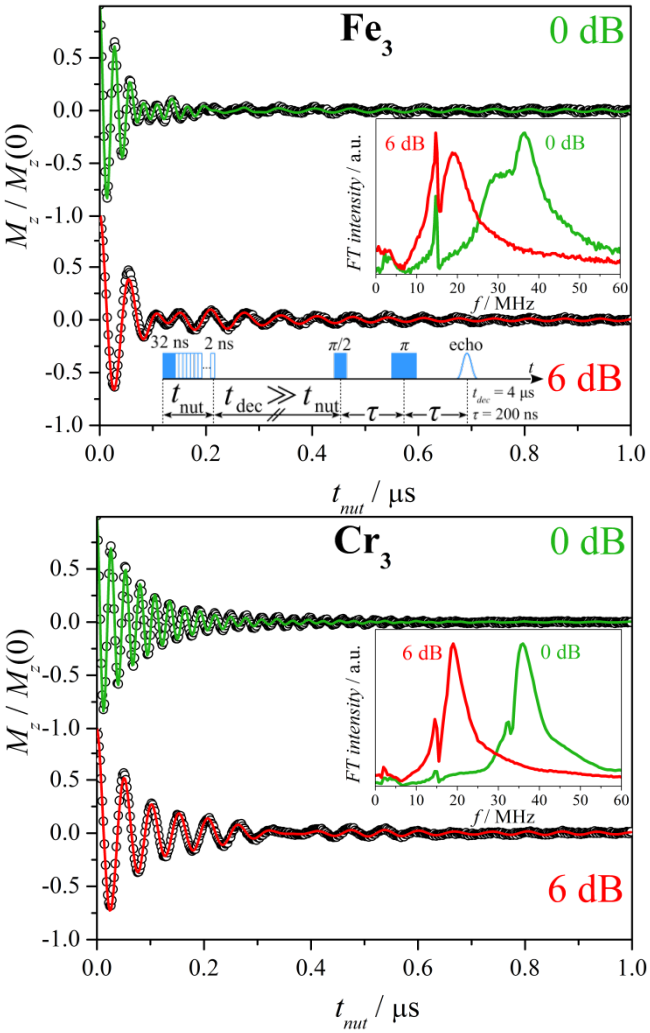


Figure 6. Nutation experimental data (o) carried out at 0 and 6 dB mw power levels on **$Fe_3$** (top panel) and **$Cr_3$** (bottom panel), showing Rabi oscillations. The lines are fits to the model described in the text. The insets show the Fourier transforms of these signals.

Table 2. Results of the fits to the nutation experiments, showing the damping times and nutation frequencies for Rabi oscillations and ESEEM oscillations at the $^1$H Larmor frequencies.

| | Att. (dB) | $\tau_{R1}$ (µs) | $\tau_{R2}$ (µs) | $\tau_H$ (µs) | $f_{R1}$ (MHz) | $f_{R2}$ (MHz) | $f_H$ (MHz) |
|---|---|---|---|---|---|---|---|
| **$Fe_3$** | 0 | 0.055(1) | 0.064(4) | 1.3(3) | 36.27(6) | 29.4(1) | 14.79(2) |
| | 6 | 0.062(1) | | 0.35(3) | 18.64(5) | | 14.8(5) |
| **$Cr_3$** | 0 | 0.059(1) | 0.16(1) | 1.2(20) | 36.63(15) | 34.7(1) | 15.0(1) |
| | 6 | 0.079(2) | 0.22(3) | 0.70(16) | 19.34(5) | 18.24(9) | 15.05(3) |

As both complexes are characterized by the same ground state total spin ($S_T$ = ½), both should exhibit the same nutation frequency under the same $|\mathbf{B}_1|$, which is proportional to $\sqrt{P}$, where $P$ is the power of the mw pulse, measured by the High Power Attenuation (HPAtt) used, and reported in dB units. It

stems that we need at least two different powers of $\mathbf{B}_1$ to ascertain the Rabi origin of the oscillations, and accordingly, two HPAtt of 6 and 0 dB were successively applied, leading to magnitudes of $|\mathbf{B}_1|$ and $2|\mathbf{B}_1|$, respectively.

Fourier transforms of the nutation traces were used to reveal the Rabi frequencies, while fits of the time-domain data to exponentially damped oscillations (equation S2) yielded their characteristic damping times. Indeed, Rabi peaks were observed for both samples with 1:2 frequency ratios (18 and 36 MHz), for 6 and 0 dB attenuation levels, respectively, confirming the nutation effect. Peaks appearing at 14.8-15.0 MHz, typical of $^1$H Larmor frequencies, were attributed to the benzoate protons, whose transitions are excited due to cross-polarization from the nearby nutation frequencies.

The main difference between the nutation traces of $\mathbf{Fe_3}$ and $\mathbf{Cr_3}$ consists in the shape of the frequency distributions. In particular, the $^1$H peak is much stronger for $\mathbf{Fe_3}$ at 6 dB attenuation, while its nutation peak is much broader at 0 dB.

For both complexes it was determined that a second Rabi frequency was required for a satisfactory fit of the time-domain data, which we attribute to slight sample and/or $\mathbf{B}_1$ inhomogeneities. To convincingly assess the origin of each peak, we carried out Fourier transforms of the data without the initial time-range where nutations are still observed. These revealed only the $^1$H Larmor frequencies whose oscillations are longer-lived (Figure S8). Indeed, at 6 dB, Rabi frequencies are no longer observed after 200 ns for $\mathbf{Fe_3}$ and after 360 ns for $\mathbf{Cr_3}$. These conclusions are in close agreement with the fits shown in Table 2, where the characteristic damping time $\tau_R$ is noticeably larger for $\mathbf{Cr_3}$.

## Discussion

Comparisons between the two complexes reveal distinct differences regarding their relaxation characteristics. The most striking of those is the large difference in $T_1$ times which, at low temperatures, is more than two orders of magnitude larger for $\mathbf{Fe_3}$ partly due to the more than double Orbach activation energy. However, it should not be neglected that spin-lattice relaxation is also much slower at the low-$T$ limit which is temperature-independent and characterized by direct processes, indicating that the $\mathbf{Cr_3}$ spins are more coupled to the phonon bath for than those of $\mathbf{Fe_3}$.

Due to this situation, the $T_1$ and $T_M$ times for each complex exhibit quite different relations at different temperatures. While the $T_1/T_M$ ratio is 146 for $\mathbf{Fe_3}$ at low temperatures (4.1 K) it is only 4.8 for $\mathbf{Cr_3}$ (4.4 K), meaning that $\mathbf{Cr_3}$ is very near the onset of a $T_1$-limited decoherence mechanism at these temperatures. At higher temperatures, this ratio changes very little for $\mathbf{Cr_3}$ (4.5 at 7 K) whereas the activation of the Orbach relaxation for $\mathbf{Fe_3}$ brings about its precipitous decrease (~3.2 near 7.5 K). Indeed, the temperature independence of $T_M$ up to 7 K for $\mathbf{Fe_3}$ indicates that decoherence at this temperature regime proceeds through spin-spin relaxation and is not $T_1$-limited.

In assessing the mechanisms through which decoherence occurs in the temperature-independent regime, comparisons between the two complexes are helpful. The main source of decoherence are the hyperfine interactions with the surrounding magnetic nuclei;[11,67] since in terms of $^1$H and $^2$H content the two complexes are identical, their differences in $T_M$ times should be sought in alternative decoherence pathways.

One such possibility are spin-spin interactions with non-excited spins, which can occur due to partial spectral excitation of very broad spectral lines. Indeed, the large spectral width of $\mathbf{Fe_3}$, consisting of strong absorptions over a 80 mT region, could point toward such a relaxation pathway. While, as will be discussed below, such a mechanism is indeed relevant for $\mathbf{Fe_3}$, its role is not pronounced in the context of Hahn echo decay experiments. Indeed, $\mathbf{Fe_3}$ exhibits strikingly similar decoherence times with $Fe_3$-salox,[5] despite the fact that the latter exhibited a much narrower spectrum (~20-30 mT) due to its nil DMI. Similarly, $\mathbf{Cr_3}$ which is characterized by a much narrower spectrum, exhibits four times faster decoherence, pointing toward other mechanisms. This means that DMI-induced spectral broadenings are not especially detrimental regarding intrinsic decoherence, as this is measured by $T_M$.

With that particular respect, an important difference between the two complexes is the content of magnetic nuclei from the metal ions themselves. Iron and chromium each possess a single stable magnetic isotope, in particular $^{57}$Fe ($I$ = ½, 2.12% abundance) and $^{53}$Cr ($I$ = 3/2, 9.50% abundance), with widely differing nuclear magnetic moments ($0.091\mu_N$ for $^{57}$Fe and $-0.47\mu_N$ for $^{53}$Cr).[68] This means that not only does $\mathbf{Fe_3}$ contain less than a quarter of magnetic nuclei with respect to $\mathbf{Cr_3}$, but that each of these exhibits about one fifth of the magnetic moment of its Cr counterpart. This difference, *ceteris paribus*, can explain the much shorter $T_M$ of $\mathbf{Cr_3}$ with respect to $\mathbf{Fe_3}$ in the temperature-independent regime.

However, a distinction needs to be made when considering the damping times of Rabi oscillations, which are found to be much shorter than $T_M$ for either complex (see Table 2). Indeed, for $T_M$ times of 2.6 μs for $\mathbf{Fe_3}$ and 0.51 μs for $\mathbf{Cr_3}$, the Rabi oscillations have fully decayed after ca. 0.20 and 0.36 μs, respectively (Figure S8). The importance of distinguishing between the two characteristic times lies with the fact that carrying out operations with qubits entails their manipulation with various methods, which introduce extrinsic decoherence sources.

In our case, i.e. that of nutation experiments, the accelerated decay is usually associated with $\mathbf{B}_1$ inhomogeneities and with incomplete spectral excitations that exacerbate decoherence through spectral diffusion. Since nutation experiments have been carried out under identical conditions and on the same instrument, we must conclude that the main driver of the observed differences should be the degree of spectral excitation, which is directly related to the spectral width. Indeed, $\mathbf{Cr_3}$ with its much narrower spectrum yields noticeably longer-lived Rabi oscillations than $\mathbf{Fe_3}$. However, in quantifying these findings in relation to DMI, we observe that for ~40 times stronger DMI, which induces a ~20 times broader spectrum (1000 vs 50 G), the Rabi oscillations of $\mathbf{Fe_3}$ still survive for about half the time of those of $\mathbf{Cr_3}$. In other words,

the 40:1 ratio in DMI only affects the Rabi oscillation survival at a ratio of ca. 2:1. This means that for a very important gain with respect to other parameters (spin chirality, magnetoelectric coupling), the detrimental effect induced by a particular type of experiment (nutations) is relatively small. This new conclusion opens the way for considering spin triangles characterized by strong DMI as viable candidates for the implementation of new technologies, such as electrically controlled spin-chirality qubits.

## Conclusions

Two structurally related spin triangles were studied using pulsed EPR techniques in order to determine their magnetic relaxation and decoherence properties, in order to assess the effect of DMI in promoting decoherence due to spectral broadenings. The kinetic parameters for both processes were extracted for each complex, whereas the observation of Rabi oscillations in nutation experiments revealed the possibility to coherently manipulate their spins. Comparisons between the two structurally similar complexes, studied in identical conditions, revealed the role of the magnetic nuclei of the metal ions in promoting intrinsic decoherence through spin-spin hyperfine interactions. At the same time, the magnetic structure of **$Fe_3$**, with its higher-energy excited states, was shown to better protect it from phonon-activated spin-lattice relaxation and, consequently, from $T_1$-induced decoherence. These same comparisons also revealed that the line broadening induced by DMI does not influence the intrinsic coherence as measured by echo decay experiments and quantified by $T_M$. In turn, it is only moderately detrimental to the coherence time as measured by nutation experiments and quantified by Rabi damping times. This last finding is particularly encouraging for further studies under electric fields, as DMI has been proposed to give rise to spin chirality and to participate in the observation of magnetoelectric coupling.[25,31] DMI should therefore be a highly advantageous mechanism in introducing valuable new quantum properties in molecular spin qubits, which could form the basis for new materials and applications.

## Experimental methods

Complexes **$Fe_3$**[28] and **$Cr_3$**[37] were prepared as previously described. Experiments were carried out on fresh py-$d_5$ solutions (2.3 mM), prepared by slight heating to accelerate dissolution and the exchange of axial py with py-$d_5$. This concentration was determined after tests as the optimal compromise for the maximization of the signal strength and the minimization of spin-spin relaxation, and was employed for the studies of both complexes to ensure comparability of the results. The solutions were deoxygenated with freeze-pump-thaw cycles, and flame-sealed under a helium atmosphere in the EPR tubes. Pulsed EPR spectra were collected at the X-band (9.75 GHz) on a Bruker ELEXSYS E580 spectrometer, fitted with an upgraded ESP1010 microwave bridge and a Bruker EN 4118X-MD4 pulse-ENDOR resonator. For low-temperature experiments the resonator was fitted in an Oxford CF935 dynamic continuous flow cryostat and the temperature was regulated with an Oxford Mercury iTC. CW EPR spectra were collected on an EMXplus spectrometer fitted with an EMX microX bridge and a Bruker ER4122SHQE cavity operating in the $TE_{011}$ mode. For low temperature experiments, the cavity was fitted with an ESR900 dynamic continuous flow cryostat controlled with an Oxford ITC503S Intelligent Temperature Controller.

FSED spectra were detected by monitoring the integrated intensity of the Hahn echo ($\pi/2$–$\tau$–$\pi$–$\tau$–echo) under varying fields. $T_1$ times were measured with inversion recovery ($\pi$–$t$–$\pi/2$–$\tau$–$\pi$–$\tau$–echo) and saturation recovery sequences. For the latter, a picket fence train of 27 $\pi/2$ pulses separated by 100 ns was used to saturate the magnetisation, before a regular Hahn echo. $T_M$ times were determined by monitoring the Hahn echo decay as a function of the incremented interpulse delay $\tau_{incr}$ ($\pi/2$–$\tau_{incr}$–$\pi$–$\tau_{incr}$–echo). Due to ESEEM, a modulation was added to the exponential decay law as described in the main text. Transient nutation experiments were carried out by applying nutation pulses of incremented duration $t_{nut}$ and by monitoring the intensity of a Hahn echo (detection block) as a function of $t_{nut}$. The Hahn echo sequence was applied after a long decoherence time $t_{dec}$ ($t_{nut}$-$t_{dec}$-$\pi/2$–$\tau$–$\pi$–$\tau$–echo). For the experiments, the delays were chosen so that $t_{dec} >> t_{nut}$ and so that the delay between two nutation sequences (shot repetition time) was larger than $3T_1$. Damping times $\tau_R$ of the Rabi oscillations were determined by fits to the time-domain data to an exponentially damped periodic function. Fourier transforms were carried out after applying a baseline correction, apodization and zero filling to the Hahn echo decay and nutation traces.

## Conflicts of interest

There are no conflicts to declare.

## Acknowledgements

This project has received funding from the European Union's Horizon 2020 research and innovation programme under the Marie Sklodowska-Curie grant agreement No 746060 (project "CHIRALQUBIT").

## References

1 M. N. Leuenberger and D. Loss, *Nature*, 2001, **410**, 789–793.

2 W. Wernsdorfer, N. Aliaga-Alcalde, D. N. Hendrickson and G. Christou, *Nature*, 2002, **416**, 406–409.

3 A. Ghirri, A. Chiesa, S. Carretta, F. Troiani, J. van Tol, S. Hill, I. Vitorica-Yrezabal, G. A. Timco, R. E. P. Winpenny and M. Affronte, *The Journal of Physical Chemistry Letters*, 2015, **6**, 5062–5066.

 

4 A. Fernandez, J. Ferrando-Soria, E. M. Pineda, F. Tuna, I. J. Vitorica-Yrezabal, C. Knappke, J. Ujma, C. A. Muryn, G. A. Timco, P. E. Barran, A. Ardavan and R. E. P. Winpenny, *Nature Communications*, 2016, **7**, 10240.
5 G. Mitrikas, Y. Sanakis, C. P. Raptopoulou, G. Kordas and G. Papavassiliou, *Phys. Chem. Chem. Phys.*, 2008, **10**, 743–748.
6 S. Bertaina, S. Gambarelli, T. Mitra, B. Tsukerblat, A. Müller and B. Barbara, *Nature*, 2008, **453**, 203–206.
7 P. Lutz, R. Marx, D. Dengler, A. Kromer and J. van Slageren, *Molecular Physics*, 2013, **111**, 2897–2902.
8 B. Kintzel, M. Böhme, J. Liu, A. Burkhardt, J. Mrozek, A. Buchholz, A. Ardavan and W. Plass, *Chemical Communications*, 2018, **54**, 12934–12937.
9 K.-Y. Choi, Z. Wang, H. Nojiri, J. van Tol, P. Kumar, P. Lemmens, B. S. Bassil, U. Kortz and N. S. Dalal, *Physical Review Letters*, , DOI:10.1103/PhysRevLett.108.067206.
10 M. Atzori, L. Tesi, E. Morra, M. Chiesa, L. Sorace and R. Sessoli, *Journal of the American Chemical Society*, 2016, **138**, 2154–2157.
11 J. M. Zadrozny, J. Niklas, O. G. Poluektov and D. E. Freedman, *ACS Central Science*, 2015, **1**, 488–492.
12 J. M. Zadrozny and D. E. Freedman, *Inorganic Chemistry*, 2015, **54**, 12027–12031.
13 K. Bader, D. Dengler, S. Lenz, B. Endeward, S.-D. Jiang, P. Neugebauer and J. van Slageren, *Nature Communications*, 2014, **5**, 5304.
14 M. J. Graham, M. D. Krzyaniak, M. R. Wasielewski and D. E. Freedman, *Inorganic Chemistry*, 2017, **56**, 8106–8113.
15 M. Atzori, S. Benci, E. Morra, L. Tesi, M. Chiesa, R. Torre, L. Sorace and R. Sessoli, *Inorganic Chemistry*, 2018, **57**, 731–740.
16 P. Becker, H.-J. Pohl, H. Riemann and N. Abrosimov, *physica status solidi (a)*, 2010, **207**, 49–66.
17 K. Saeedi, S. Simmons, J. Z. Salvail, P. Dluhy, H. Riemann, N. V. Abrosimov, P. Becker, H.-J. Pohl, J. J. L. Morton and M. L. W. Thewalt, *Science*, 2013, **342**, 830–833.
18 E. Moreno-Pineda, C. Godfrin, F. Balestro, W. Wernsdorfer and M. Ruben, *Chemical Society Reviews*, 2018, **47**, 501–513.
19 C. Godfrin, A. Ferhat, R. Ballou, S. Klyatskaya, M. Ruben, W. Wernsdorfer and F. Balestro, *Physical Review Letters*, , DOI:10.1103/PhysRevLett.119.187702.
20 S. Bertaina, S. Gambarelli, A. Tkachuk, I. N. Kurkin, B. Malkin, A. Stepanov and B. Barbara, *Nature Nanotechnology*, 2007, **2**, 39–42.
21 S. Thiele, F. Balestro, R. Ballou, S. Klyatskaya, M. Ruben and W. Wernsdorfer, *Science*, 2014, **344**, 1135–1138.
22 R. Hussain, G. Allodi, A. Chiesa, E. Garlatti, D. Mitcov, A. Konstantatos, K. S. Pedersen, R. De Renzi, S. Piligkos and S. Carretta, *Journal of the American Chemical Society*, 2018, **140**, 9814–9818.
23 D. A. Lidar, I. L. Chuang and K. B. Whaley, *Physical Review Letters*, 1998, **81**, 2594–2597.
24 M. Trif, F. Troiani, D. Stepanenko and D. Loss, *Physical Review Letters*, 2008, **101**, 217201.
25 M. Trif, F. Troiani, D. Stepanenko and D. Loss, *Physical Review B*, 2010, **82**, 045429.
26 F. Troiani, D. Stepanenko and D. Loss, *Physical Review B*, 2012, **86**, 161409(R).
27 D. Stepanenko, M. Trif, O. Tsyplyatyev and D. Loss, *Semiconductor Science and Technology*, 2016, **31**, 094003.
28 A. K. Boudalis, J. Robert and P. Turek, *Chemistry - A European Journal*, 2018, **24**, 14896–14900.
29 J. Liu, J. Mrozek, W. K. Myers, G. A. Timco, R. E. P. Winpenny, B. Kintzel, W. Plass and A. Ardavan, *Physical Review Letters*, 2019, **122**, 037202.
30 M. I. Belinsky, *Chemical Physics*, 2014, **435**, 62–94.
31 M. I. Belinsky, *Chemical Physics*, 2014, **435**, 95–125.
32 A. K. Boudalis, Y. Sanakis, F. Dahan, M. Hendrich and J.-P. Tuchagues, *Inorganic Chemistry*, 2006, **45**, 443–453.
33 A. N. Georgopoulou, Y. Sanakis and A. K. Boudalis, *Dalton Transactions*, 2011, **40**, 6371.
34 A. N. Georgopoulou, I. Margiolaki, V. Psycharis and A. K. Boudalis, *Inorganic Chemistry*, 2017, **56**, 762–772.
35 L. Mathivathanan, A. K. Boudalis, P. Turek, M. Pissas, Y. Sanakis and R. G. Raptis, *Physical Chemistry Chemical Physics*, 2018, **20**, 17234–17244.
36 A. Schweiger and G. Jeschke, *Principles of pulse electron paramagnetic resonance*, Oxford University Press, Oxford, UK ; New York, 2001.
37 A. K. Boudalis, G. Rogez and P. Turek, *Inorganic Chemistry*, 2018, **57**, 13259–13269.
38 K. Kambe, *Journal of the Physical Society of Japan*, 1950, **5**, 48–51.
39 J. Yvon, J. Horowitz and A. Abragam, *Reviews of Modern Physics*, 1953, **25**, 165–165.
40 J. Wucher and H. M. Gijsman, *Physica*, 1954, **20**, 361–366.
41 G. J. Long, W. T. Robinson, W. P. Tappmeyer and D. L. Bridges, *J. Chem. Soc., Dalton Trans.*, 1973, 573–579.
42 T. Murao, *Physics Letters A*, 1974, **49**, 33–35.
43 D. H. Jones, J. R. Sams and R. C. Thompson, *The Journal of Chemical Physics*, 1984, **81**, 440.
44 Yu. V. Rakitin, V. T. Kalinnikov and V. M. Novotortsev, *Russian Chemical Bulletin*, 2004, **53**, 2478–2484.
45 Yu. V. Rakitin, Yu. V. Yablokov and V. V. Zelentsov, *Journal of Magnetic Resonance (1969)*, 1981, **43**, 288–301.
46 B. Tsukerblat, M. Belinskii and V. Fainzil'berg, *Soviet Sci. Rev. B, Harwood Acad. Pub*, 1987, 337–482.
47 H. Nishimura and M. Date, *Journal of the Physical Society of Japan*, 1985, **54**, 395–399.
48 M. Honda, M. Morita and M. Date, *Journal of the Physical Society of Japan*, 1992, **61**, 3773–3785.
49 Y. Sanakis, A. L. Macedo, I. Moura, J. J. G. Moura, V. Papaefthymiou and E. Münck, *Journal of the American Chemical Society*, 2000, **122**, 11855–11863.
50 S. Ferrer, F. Lloret, E. Pardo, J. M. Clemente-Juan, M. Liu-González and S. García-Granda, *Inorganic Chemistry*, 2012, **51**, 985–1001.
51 B. Guigliarelli, J. P. Gayda, P. Bertrand and C. More, *Biochimica et Biophysica Acta (BBA) - Protein Structure and Molecular Enzymology*, 1986, **871**, 149–155.
52 B. Guigliarelli, C. More, P. Bertrand and J. P. Gayda, *The Journal of Chemical Physics*, 1986, **85**, 2774–2778.
53 N. Uryû and S. A. Friedberg, *Physical Review*, 1965, **140**, A1803–A1811.

54 M. Sorai, M. Tachiki, H. Suga and S. Seki, *Journal of the Physical Society of Japan*, 1971, **30**, 750–759.
55 A. J. Fielding, S. Fox, G. L. Millhauser, M. Chattopadhyay, P. M. H. Kroneck, G. Fritz, G. R. Eaton and S. S. Eaton, *Journal of Magnetic Resonance*, 2006, **179**, 92–104.
56 D. A. Garanin, *Physical Review B*, , DOI:10.1103/PhysRevB.75.094409.
57 J. Pescia, *Journal de Physique*, 1966, **27**, 782–800.
58 H. J. Stapleton, in *Energy Transfer Dynamics*, eds. T. W. Barrett and H. A. Pohl, Springer Berlin Heidelberg, Berlin, Heidelberg, 1987, pp. 210–223.
59 H.-Y. Ko, R. A. DiStasio, B. Santra and R. Car, *Physical Review Materials*, 2018, **2**, 055603.
60 J. Telser, H.-I. Lee and B. M. Hoffman, *JBIC Journal of Biological Inorganic Chemistry*, 2000, **5**, 369–380.
61 M. Atzori, A. Chiesa, E. Morra, M. Chiesa, L. Sorace, S. Carretta and R. Sessoli, *Chemical Science*, 2018, **9**, 6183–6192.
62 F. Moro, D. Kaminski, F. Tuna, G. F. S. Whitehead, G. A. Timco, D. Collison, R. E. P. Winpenny, A. Ardavan and E. J. L. McInnes, *Chem. Commun.*, 2014, **50**, 91–93.
63 A. Ardavan, O. Rival, J. J. L. Morton, S. J. Blundell, A. M. Tyryshkin, G. A. Timco and R. E. P. Winpenny, *Physical Review Letters*, 2007, **98**, 057201.
64 A. Ardavan, A. M. Bowen, A. Fernandez, A. J. Fielding, D. Kaminski, F. Moro, C. A. Muryn, M. D. Wise, A. Ruggi, E. J. L. McInnes, K. Severin, G. A. Timco, C. R. Timmel, F. Tuna, G. F. S. Whitehead and R. E. P. Winpenny, *npj Quantum Information*, , DOI:10.1038/npjqi.2015.12.
65 D. Kaminski, A. L. Webber, C. J. Wedge, J. Liu, G. A. Timco, I. J. Vitorica-Yrezabal, E. J. L. McInnes, R. E. P. Winpenny and A. Ardavan, *Physical Review B*, , DOI:10.1103/PhysRevB.90.184419.
66 C. J. Wedge, G. A. Timco, E. T. Spielberg, R. E. George, F. Tuna, S. Rigby, E. J. L. McInnes, R. E. P. Winpenny, S. J. Blundell and A. Ardavan, *Physical Review Letters*, , DOI:10.1103/PhysRevLett.108.107204.
67 M.-X. Xu, Z. Liu, B.-W. Dong, H.-H. Cui, Y.-X. Wang, J. Su, Z. Wang, Y. Song, X.-T. Chen, S.-D. Jiang and S. Gao, *Inorganic Chemistry*, 2019, **58**, 2330–2335.
68 N. J. Stone, *Atomic Data and Nuclear Data Tables*, 2005, **90**, 75–176.

 